# A Mechanism-Data Driven Self-Adaptive Online Estimation Algorithm for 3-D Temperature Distribution of Battery

Yi Xie, *Member, IEEE*, Wensai Ma, Wei Li, *Member, IEEE*, Rui Yang, Xiaoqiong Hu, Yonggang Luo, and Yangjun Zhang

***Abstract*—Lithium batteries receive widespread attention as core components in electric vehicles, with their performance being significantly influenced by temperature. To enable accurate online estimation of battery temperature, this article proposes a self-adaptive 3-D thermal modeling method. The model's self-adaptation is achieved through a two-step resistance transfer algorithm (RTA). First, a linear relationship between temperature and battery resistance is established based on the Arrhenius equation. This relationship is used to calibrate the migration coefficient from the reference battery resistance to the target battery resistance. Second, the heat generation model of the target battery is updated based on this migration coefficient to achieve thermal model self-adaptation. For precise online temperature estimation, a 3-D thermal conduction equation is solved in place of a lumped parameter model, and a thermal resistance network is developed to simplify the equation and expedite the solution process. This network divides the battery into microstructures and refines the heat transfer relationships of these microstructures using the first law of thermodynamics. Based on these models, we propose a mechanism-data-driven self-adaptive algorithm to accurately compute the battery's 3-D temperature distribution online. Testing on different batteries shows that RTA achieves accurate resistance transfer with a maximum error below 0.0341 mΩ, whereas the online thermal model estimates temperature distribution with a computation time of 0.496 s and an error below 1.515 °C. Additionally, the comparison results demonstrate that this method (0.496 s) is significantly more efficient than the finite element method (2662.33 s) in terms of computation time.**

***Index Terms*—Electric vehicle, lithium-ion battery, online electrothermal modeling, resistance transfer algorithm (RTA), 3-D thermal resistance network.**

Received 15 December 2024; accepted 14 January 2025. Date of publication 20 January 2025; date of current version 26 February 2025. This work was supported in part by the National Key Research and Development Program under Grant 2022YFB3305400 and Grant 2021YFE0193800, in part by the NSF of China under Grant 52472375, Grant U20A20310, Grant 52202434, and Grant 52072052, in part by the State Key Laboratory of Intelligent Green Vehicle and Mobility (KFZ2404), and in part by the Chongqing Science and Technology Commission under Grant CSTB2023NSCQ-LZX0170. Recommended for publication by Associate Editor H. Chaoui. *(Corresponding authors: Yi Xie; Yangjun Zhang.)*

Yi Xie and Wensai Ma are with the College of Mechanical and Vehicle Engineering, Chongqing University, Chongqing 400044, China (e-mail: claudexie@cqu.edu.cn; wensai_ma@stu.cqu.edu.cn).

Wei Li is with the College of Design and Engineering, National University of Singapore, Singapore 117575 (e-mail: l-w94@ieee.org).

Rui Yang is with the School of Energy and Power Engineering, Chongqing University, Chongqing 400044, China (e-mail: 20211001004@stu.cqu.edu.cn).

Xiaoqiong Hu and Yonggang Luo are with the AI Lab, Chongqing Changan Automobile Ltd., Chongqing 401133, China (e-mail: huxq1@changan.com.cn; luoyg3@changan.com.cn).

Yangjun Zhang is with the State Key Laboratory of Automotive Safety and Energy, Tsinghua University, Beijing 100084, China (e-mail: yjzhang@tsinghua.edu.cn).

Color versions of one or more figures in this article are available at https://doi.org/10.1109/TPEL.2025.3531851.

Digital Object Identifier 10.1109/TPEL.2025.3531851

## NOMENCLATURE

### A. Parameters

| | |
|---|---|
| $R_T$ | Resistance of the battery. |
| $E_a$ | Active energy. |
| $R$ | Gas constant. |
| $T$, $T_a$ | Temperature of the battery and ambient. |
| SOC | Battery SOC value. |
| $a$ | Slope of the linearized resistance. |
| $b$ | Intercept of the linearized resistance. |
| $K_a$ | Slope ratio of the target and original battery. |
| $K_b$ | Intercept ratio of the target and original battery. |
| $\mathrm{RE}_{\mathrm{ave}}$ | Average relative error. |
| $V_{\mathrm{ar}}$ | Variance. |
| $Q$ | Heat generation rate. |
| $U_{\mathrm{OCV}}$, $V$, $I$ | Terminal voltage, voltage, and current of the battery. |
| $M_A$, $V_A$ | Mass and volume of zone A. |
| $\rho$, $C_p$ | Density and specific heat capacity of the battery. |
| $R_t$ | Heat resistance. |
| $d$ | Effective distance between the microstructure. |
| $s$ | Surface area of the microstructure. |
| $k$ | Thermal conductivity coefficient. |
| $h$ | Heat exchange coefficient. |
| $dU_{\mathrm{OCV}}/dT$ | Entropy heat coefficient. |

### B. Abbreviations

| | |
|---|---|
| EVs | Electric vehicles. |
| SOC | State of charge. |
| SOH | State of health. |
| SOT | State of temperature. |
| SOTD | State of temperature distribution. |
| BTMS | Battery thermal management systems. |
| LTM | Lumped-parameter thermal model. |
| PA | Polynomial approximation. |
| HPPC | Hybrid pulse power characteristic. |

| | |
|---|---|
| FEM | Finite element method. |
| RTA | Resistance transfer algorithm. |
| TRN | Thermal resistance network. |
| LRM | Linearized resistance model. |
| MAE | Mean absolute error. |

## I. Introduction

ELECTRIC vehicles (EVs) have become an important development direction of the world's transport carriers with the advantages of energy conservation and environmental protection [1], [2]. Lithium batteries, due to their high specific energy, high power density, and long service life, are considered the best solution for energy storage systems of EVs [3]. Although lithium batteries have become commonplace as the power unit of EVs, there are still many issues that plague the safety and stability of lithium batteries, such as poor low-temperature performance and thermal runaway [4], [5], [6]. Meanwhile, owing to the sealed nature of the battery, key parameters including state of charge (SOC), state of health (SOH), internal resistance, and core temperature cannot be directly obtained through simple measurements, except for a few parameters such as current and voltage [7], [8], [9]. For the above critical state parameters of the battery, SOC, SOH, and resistance are all affected by the battery temperature [10]. The optimal performance of the battery also depends on its operating temperature [11], [12]. However, the gradual increase in the size of the battery and the inhomogeneous heat transfer characteristics make it difficult to accurately obtain the state of temperature (SOT) of the battery core [13]. Therefore, accurate SOT distribution (SOTD) reconstruction is needed to obtain the precise temperature field of the battery. It enables the provision of reliable SOT information for battery thermal management systems (BTMS) and has an important role in the battery management of EVs [14].

The reconstruction of SOTD mainly relies on the heat generation model and heat conduction model, they are collectively referred to as the thermal model [15], [16]. Currently, thermal models can be classified into online and offline thermal models, depending on the modeling process and operating characteristics. For the online thermal model, the parameter identification method is utilized to obtain the resistance parameter based on the current and the voltage [15]. The heat generation model of the battery is then constructed based on the identified resistance and Bernardi equation. For example, Shi et al. [17] constructed a thermal characteristic model of the battery and the forgetting factor recursive least squares algorithm is used to realize the online identification of the parameters of the lumped thermal characteristic model. Li et al. [18] applied the auxiliary model modified forgetting gradient algorithm to verify the battery resistance online. Wang et al. [19] used the parameter identification model based on the limited memory recursive least squares to get the resistance online. However, this sort of method is based on a certain operating condition to achieve parameter identification; the parameter is fixed values and generally tied to operating condition attributes, and it cannot adapt to different SOCs and temperatures. Therefore, this type of method is subject to accuracy errors when used for heat generation calculations different from the identified operating conditions. In terms of heat transfer, online thermal modeling needs to avoid complex arithmetic, thus, simplifying the heat transfer relationship is necessary. The main simplification methods are the lumped parameter method and the model reduction method. He et al. [20] implemented temperature simulation analysis under the 1-D level using a lumped-parameter model, with a maximum error of 4.5% but a significant increase in computational speed, it only requires 3.9% of the time used by the computational fluid dynamics (CFD) model. Song et al. [21] implemented the core and case temperature prediction based on a lumped-parameter thermal model (LTM), and the predicted temperature is validated based on a homemade small soft pack battery with a relative error of no more than 5%. The LTM improves computational efficiency, but it directly ignores the internal heat transfer information of the battery, which will produce a large error in the temperature prediction of high-rate charge/discharge for large-volume batteries. The model reduction method is common in distributed thermal models, and it simplifies the 3-D battery temperature field by the polynomial approximation (PA). Richardson and Howey [22] used the PA method to achieve a reduced order of the cylindrical heat equation. The PA method ignores the heat conduction process and the influence of the BTMS. Due to its substantial simplification, it is difficult to accurately diagnose the battery temperature field information and adapt to different operation conditions. For the offline thermal model, resistances are tested at different temperatures and SOCs via the hybrid pulse power characteristic (HPPC) experiment to construct the multiparameter resistance response surface model, and the heat generation model is established based on the offline resistance model. Xie et al. [23] conducted extensive HPPC tests to obtain resistances at different temperatures and SOCs for a reasonable heat generation model based on the Bernardi equation and solved the thermal conduction by the finite element method (FEM). Despite the high accuracy of the model, it is developed only for specific batteries and cannot be adapted to other batteries to complete online adaptation. The offline heat conduction model mainly uses the FEM to solve the 3-D temperature field. For example, Pordanjani et al. [24] explored the effect of a cooling system on electrochemical-thermal performance when batteries are designed in various configurations based on the FEM. The advantage of FEM is its high accuracy, albeit at the cost of extensive calculations. Therefore, the FEM is usually used in battery design and cannot be applied in online scenarios.

In summary, the problems that need to be solved for the high-precision online solution of the 3-D temperature field are as follows: 1) accurate online modeling of battery internal resistance and 2) fast calculation of the thermal conductivity equation for the 3-D temperature field. Given the above problems, a self-adaptive 3-D online thermal model is proposed based on the resistance transfer algorithm (RTA) and the 3-D thermal resistance network (TRN). The proposed RTA enables online self-adaptation for the resistance-based heat generation model. The thermal conduction network model achieves efficient 3-D temperature field reconstruction by simplifying the calculation of heat conduction, which allows the 3-D thermal model for online applications.

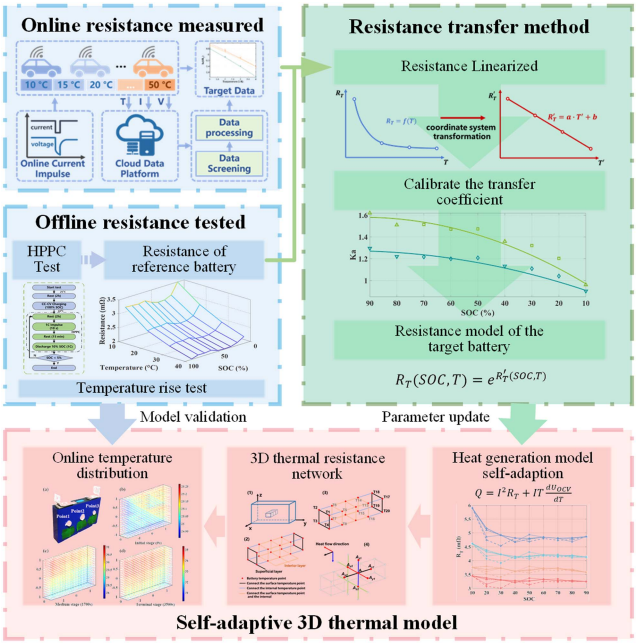


Fig. 1. Flowchart of the main procedure.

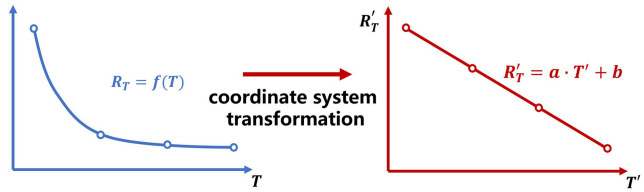


Fig. 2. Coordinate system transformation diagram.

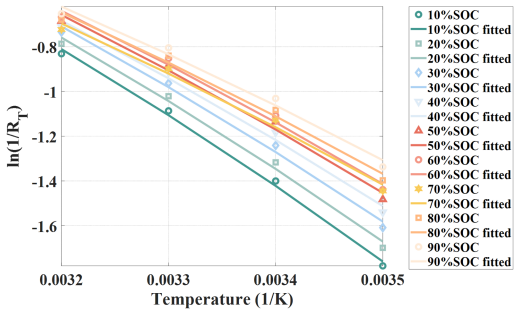


Fig. 3. LRM of LFP (25 Ah) at different SOCs.

The main contributions of the study can be listed as follows.

1) Constructing a generalized representation of battery internal resistance with respect to SOC and temperature based on the linearized Arrhenius equation.
2) The RTA is proposed, offline data combined with a migration coefficient calibration algorithm of RTA enables highly accurate online modeling of the battery heat generation model.
3) To realize online 3-D heat conduction calculation, the 3-D TRN is proposed to discretize the battery, it preserves the heat transfer characteristics inside the battery and enables fast calculation of the 3-D temperature field with the calculation durations of different batteries no more than 0.496 s.

The main procedural steps of this study are shown in Fig. 1.

The rest of this article is organized as follows. Section II describes the general expression of battery resistance and the experiment profiles. Section III introduces RTA and its application to the heat generation model. Section IV introduces the 3-D thermal model based on the TRN. Section V validates the application effect of the 3-D thermal model. Finally, Section VI concludes this article.

## II. General Expression of Battery Resistance and Experiment

### A. Linearized Resistance Model Based on Arrhenius Equation

Researchers have identified that the relationship between the electrochemical processes and the temperature of the lithium battery can be described by the Arrhenius equation [25]. Meanwhile, battery resistance shows a high correlation with electrochemical processes [25], [26]. Therefore, researchers explored the following relationship between the temperature and the battery resistance based on the Arrhenius equation [27]:

$$\frac{1}{R_T} = K \cdot \exp\left(-\frac{E_a}{RT}\right) \tag{1}$$

where $R_T$ is the resistance of the battery, $E_a$ is the active energy, $R$ is the gas constant, $T$ is the Kelvin temperature of the battery, and $K$ is a constant. It can be expressed as

$$\ln\left(\frac{1}{R_T}\right) = \left(-\frac{E_a}{R}\right) \cdot \frac{1}{T} + \ln K \tag{2}$$

such that

$$\begin{cases} \ln\left(\frac{1}{R_T}\right) = R' \\ \frac{1}{T} = T' \end{cases}. \tag{3}$$

The linear relationship can be found more intuitively through the coordinate system transformation as shown in Fig. 2, and the linearized resistance model (LRM) can be expressed as

$$R_T' = a \cdot T' + b \tag{4}$$

where

$$\begin{cases} a = -\frac{E_a}{R} \\ b = \ln K \end{cases}. \tag{5}$$

### B. General Expression of Battery Resistance at Different Temperatures and SOCs

As shown in Fig. 3, the relationship between the battery resistance and the temperature can be illustrated by (4). However, in addition to temperature, the SOC of the battery is another important factor affecting battery resistance. Therefore, to obtain a complete model of the internal resistance of the battery, it is necessary to derive a generalized expression for the internal resistance of the battery at different SOCs and temperatures.

The LRM at different SOC states can be expressed by a cluster of similar straight lines, as shown in Fig. 3. To obtain a general

TABLE I
TECHNICAL SPECIFICATIONS OF BATTERIES

| Battery | Cathode material | Anode material | Rated capacity (Ah) | Mass(g) | Dimension (mm) L*H*T | Rated voltage (V) |
|---|---|---|---|---|---|---|
| NCM111 | $LiNi_{1/3}Co_{1/3}Mn_{1/3}O_2$ | Graphite | 5.5 | 210 | 120*65*12.5 | 3.65 |
| NCM523 | $LiNi_{0.5}Co_{0.2}Mn_{0.3}O_2$ | Graphite | 102 | 1700 | 148.9*95.8*52.2 | 3.7 |
| NCM622 | $LiNi_{0.6}Co_{0.2}Mn_{0.2}O_2$ | Graphite | 50 | 895 | 148.3*98*26.7 | 3.65 |
| NCM622 | $LiNi_{0.6}Co_{0.2}Mn_{0.2}O_2$ | Graphite | 51 | 835 | 148*91.4*26.7 | 3.65 |
| NCM811 | $LiNi_{0.8}Co_{0.1}Mn_{0.1}O_2$ | Graphite | 120 | 1730 | 301*91.5*27 | 3.7 |
| LFP | $LiFePO_4$ | Graphite | 25 | 650 | 100*141*21 | 3.2 |
| LFP | $LiFePO_4$ | Graphite | 8 | 330 | 160*227*4.8 (Pouch) | 3.3 |

expression of resistance at different SOCs and temperatures, a polynomial is used to fit the relationship between $a$, $b$, and SOC, so (4) is changed into the following equation:

$$R_T'(\mathrm{SOC}, T) = a(\mathrm{SOC}) \cdot T' + b(\mathrm{SOC}) \tag{6}$$

where

$$\begin{cases} a(SOC) = \sum_i^n c_i \cdot \mathrm{SOC}^i + C_1 \\ b(SOC) = \sum_i^n d_i \cdot \mathrm{SOC}^i + C_2 \end{cases}. \tag{7}$$

Equation (6) establishes a general representation of battery internal resistance at different SOCs and temperatures. It is the basis for performing the RTA, and the resistance of the battery at a certain SOC and temperature can be calculated by

$$R_T(\mathrm{SOC}, T) = e^{R_T'(\mathrm{SOC}, T)}. \tag{8}$$

### C. Date Preparation

Battery experiments are necessary to obtain the total resistance at different temperatures and different SOCs and evaluate the proposed method. Researchers found by comparing that the resistance obtained by the HPPC method for battery thermal modeling has better performance [28], and the online internal resistance used for RTA is also based on pulsed currents. Therefore, the HPPC test is conducted to obtain the total resistance of the battery. The test is performed at different temperatures (10 °C, 20 °C, 30 °C, 40 °C) and different SOCs (90% SOC to 10% SOC with an interval of 10%). The impulse current is 1 C (C-rate is the measurement of the current with respect to its nominal capacity). In this article, NCM111, NCM523, NCM622, NCM811, and LFP batteries are tested, and the technical specifications are shown in Table I.

As shown in Fig. 4(a), Neware BTS-8000 (5 V, 100 A) is used as the battery tester, and its measurement accuracy is ±0.1%. The temperature control accuracy of the thermostat is ±0.5 °C. The battery surface temperature is collected by a Keysight 34970A temperature collector with K-type thermocouples with an error of ±0.75%. The battery is charged with CC-CV mode at 25 °C with 1 C constant current, then the HPPC and temperature rise test are performed at a set temperature, respectively. The test flowchart of HPPC is shown in Fig. 4(b), the detailed test procedure of two SOC stages (90%SOC and 80% SOC) is shown in Fig. 4(c), $R_o$ is the ohmic resistance and $R_p$ is the polarization resistance, and the total internal resistance is the sum of $R_o$ and $R_p$. The NCM811 uses parallel channels due to its large capacity, and the HPPC voltage drop is detailed in Fig. 4(e). The detail of the temperature rise test at 25 °C is demonstrated in Fig. 4(d), and the test results at different C-rates are shown in Fig. 4(f).

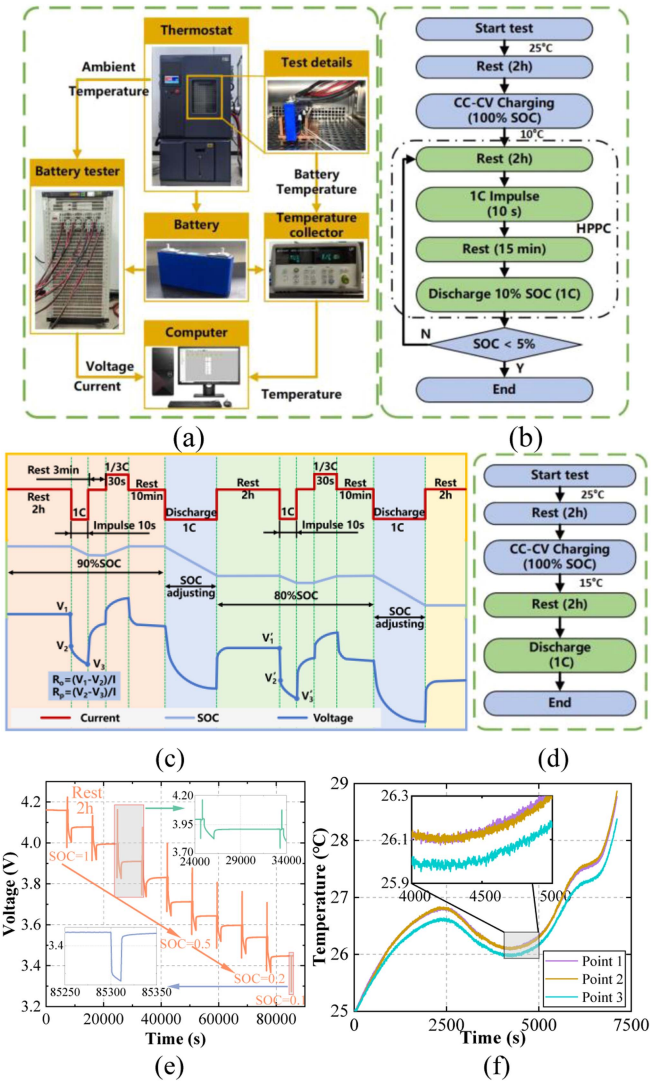


Fig. 4. Battery test flowchart and procedure. (a) Experimental setup. (b) Test flowchart of HPPC. (c) Detailed HPPC test procedure. (d) Test flowchart of temperature rise. (e) HPPC voltage drop of NCM811. (f) Temperature profile of NCM622 during 1 C discharge at 25 °C.

## III. RESISTANCE TRANSFER ALGORITHM AND ITS APPLICATION TO ONLINE HEAT GENERATION MODEL

The research aims to realize the online application and self-adaption of the thermal model, and the online self-adaptation of model parameters is one of the key problems to be solved. Therefore, the RTA is proposed. The framework consists of the following three components:

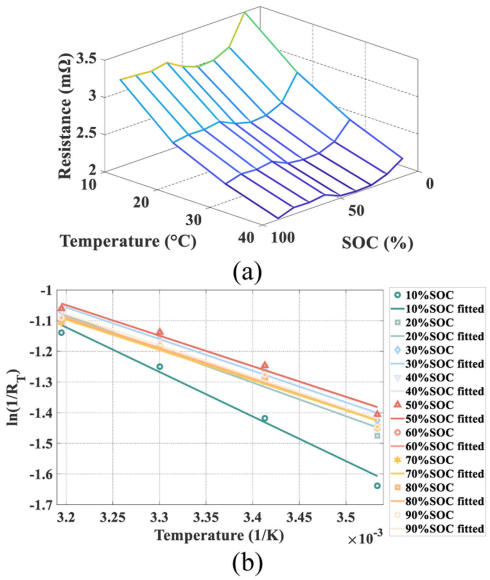


Fig. 5. Resistance and LTM at different SOC and temperatures. (a) Tested resistances of the target battery. (b) LRM of the battery at different SOCs.

1) high-precision resistance modeling and linear generalization for the original battery;
2) online acquisition of the target battery's resistances at specific states; and
3) resistance calibration based on the source battery's resistance model and the target battery's partial resistance data.

### A. Original Battery Resistances and Its Generalization

The internal resistance of the target battery is migrated from the internal resistance of the original battery. Thus, the internal resistance of the original battery needs to be tested in detail. In this study, the NCM622 (50 Ah) battery is leveraged as the original battery, and its tested resistances as shown in Fig. 5(a).

According to the generalization methods in Section II, the LRM of the battery at different SOC are fitted, the LRM results are shown in Fig. 5(b). Then, the resistance general expression of the original battery can be obtained by fitting the slope $a$ and intercept $b$ at different SOCs

$$\begin{cases} a\,(SOC) = \sum_{i=0}^{6} c_i \cdot \mathrm{SOC}^i \\ b\,(SOC) = \sum_{i=0}^{6} d_i \cdot \mathrm{SOC}^i \end{cases}. \tag{9}$$

$R'_{\mathrm{ori}}$ can be expressed as

$$R'_{\mathrm{ori}}\,(\mathrm{SOC}, T) = \sum_{i=0}^{6} c_i \cdot \mathrm{SOC}^i \cdot T' + \sum_{i=0}^{6} d_i \cdot \mathrm{SOC}^i. \tag{10}$$

The coefficient matrices $c_i$ and $d_i$ are as follows:

$$c_i = [239.7, -624.2648.3, -343.7, 99.15, \\ -14.81, 2.96]^T \tag{11}$$

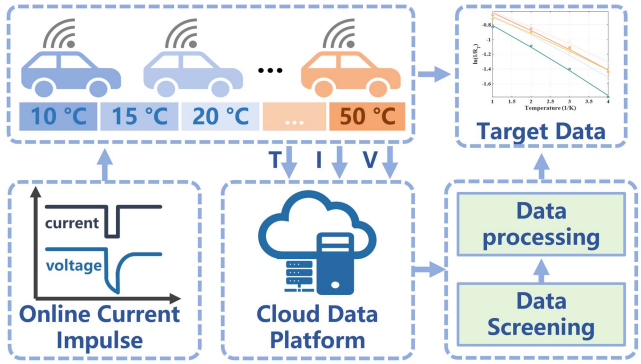


Fig. 6. Online resistance acquisition method.

$$d_i = \begin{bmatrix} -8.676 \times 10^4 \\ 2.338 \times 10^5 \\ -2.517 \times 10^5 \\ 1.375 \times 10^5 \\ -3.996 \times 10^4 \\ 5.183 \times 10^3 \\ -1.316 \times 10^3 \end{bmatrix}. \tag{12}$$

The model serves as an offline database to provide a raw database for calibrating the internal resistance model of the target battery.

### B. Online Measurement of the Target Battery Resistance

For the online adaptive thermal model, the resistance test at the laboratory cannot meet the requirements of online modeling, including changes in temperature and operating conditions and test time requirements. Therefore, an alternative method for online resistance calculation is needed. In this study, inspired by the ac pulse heating theory, a method of leveraging a cloud data platform is used for resistance calculation. As shown in Fig. 6, to quickly obtain the online resistances at different temperatures and SOCs, it is possible to apply a current impulse at the start moment of EVs. The data can be collected, screened, and processed by the cloud data platform, and the resistance can be calculated. After obtaining the resistance data at the desired SOC conditions, such as [90%, 80%, 40%, 10%], the online resistance at certain temperatures and SOCs of the target battery can serve as the online database, the resistance of the original battery serves as the offline database. Then, the resistance of the target battery can be calculated using the RTA method. Based on the resistance calculated by the RTA, the resistance parameter of the heat generation model can be updated.

### C. Calibration Based on Online Resistance Data

For the target battery, the SOC points at 90% state and 10% state are necessary, and the rest of the SOC points are alternatives. The selected SOC points can be 1, 2, or 3, corresponding, respectively, to the options listed in Table II as 3-SOC scheme, 4-SOC scheme, and 5-SOC scheme.

Taking the 4-SOC scheme as an example, excepting 90% SOC and 10% SOC, two of the remaining seven SOC points are needed. As shown in Table II, the number of schemes that can be chosen is 21. Assuming that one of the 4-SOC schemes,

TABLE II
TEST SOC POINTS OF DIFFERENT SCHEMES

| Schemes | 3-SOC Scheme | 4-SOC Scheme | 5-SOC Scheme |
|---|---|---|---|
| SOC points | 3 | 4 | 5 |
| Number of schemes | $C_7^1 = 7$ | $C_7^2 = 21$ | $C_7^3 = 35$ |

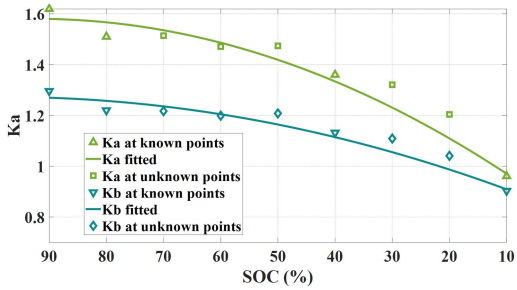


Fig. 7. $K_a$ and $K_b$ of the NCM622(51 Ah) battery.

SOC = [90%, 80%, 40%, 10%] is selected. First, the linear fitting of the resistances at the four SOCs is obtained by (6), and $K_a$ and $K_b$ in the following equation are calculated:

$$\begin{cases} K_a = \frac{a_{\text{tar}}}{a_{\text{ori}}} \\ K_b = \frac{b_{\text{tar}}}{b_{\text{ori}}} \end{cases} \tag{13}$$

where $a_{\text{tar}}$ and $b_{\text{tar}}$ are the slope and intercept of the target battery in (6), and $a_{\text{ori}}$ and $b_{\text{ori}}$ can be calculated by (9). Second, $K_a$(SOC) and $K_b$(SOC) of the target battery are fitted by using the least-squares fitting method. Fig. 7 shows the fitted results. Third, $K_a$ and $K_b$ of the target battery at unmeasured SOCs (SOC = [70%, 60%, 50%, 30%, 20%]) can be conducted by substituting the SOCs into $K_a$(SOC) and $K_b$(SOC). Finally, based on (13), the slopes and intercepts of (6) at unmeasured SOCs can be calculated, and the LRM at all SOC and the resistance general expression of the target battery can be obtained.

### D. Validation of RTA

To validate the feasibility of the RTA and contrast the proposed three different schemes, we compared the true values with the internal resistance obtained by RTA. All the 63 schemes in Table II are tried and filtered to give the optimal scheme. The average relative error ($\text{RE}_{\text{ave}}$) and the variance ($V_{\text{ar}}$) are used to evaluate the precision and dispersion of the RTA for different batteries.

$$\text{RE}_{\text{ave}} = \frac{1}{N_1} \sum_{i=1}^{N_1} \left( \frac{R_{T,p,i} - R_{T,e,i}}{R_{T,e,i}} \right) \times 100\% \tag{14}$$

$$V_{\text{ar}} = \frac{1}{N_2} \sum_{i=1}^{N_2} \left( \text{RE}_{\text{ave},i} - \overline{\text{RE}_{\text{ave}}} \right)^2 \tag{15}$$

where $N_1$ is the number of the predicted resistances, $R_{T,p,i}$ is the predicted resistance points, and $R_{T,e,i}$ is the experiment resistance points. $N_2$ is the number of the batteries, $\text{RE}_{\text{ave},i}$ is the $\text{RE}_{\text{ave}}$ of the battery, and $\overline{\text{RE}_{\text{ave}}}$ represents the average $\text{RE}_{\text{ave}}$ of all batteries. $V_{\text{ar}}$ can evaluate the dispersion n of errors in different schemes and filter out the optimal one.

All errors of the 3-SOC scheme are given in Table III, and due to space constraints, only the optimal solutions for the 4-SOC scheme and the 5-SOC scheme are given in Table IV. Meanwhile, the results of the real resistance values contrast with RTA values are shown in Fig. 8. According to Table III, the scheme of test point at SOC = [90%, 40%, 10%] is the best scheme of all 3-SOC schemes, which has minimal $\overline{\text{RE}_{\text{ave}}}$ (4.80%) and $V_{ar}$ (0.01%). In the scheme, the maximum $\text{RE}_{\text{ave}}$ is 5.76% of the LFP (8 Ah) battery, whereas the real resistance value difference is only 0.0341 mΩ (5.92 mΩ×5.76%). Meanwhile, for LFP (8 Ah), a comparison of other schemes points out that the scheme SOC = [90%, 50%, 10%] has the smallest $\text{RE}_{\text{ave}}$ (4.67%). This indicates that the scheme of SOC = [90%, 40%, 10%] is general for all batteries, whereas there may be better options for individual batteries.

The schemes of test point at SOC = [90%, 60%, 30%, 10%] and SOC = [90%, 70%, 60%, 30%, 10%] are the optimal solution of the 4-SOC scheme and 5-SOC scheme, respectively. A comparison of the three optimal solutions shows that an increase in the number of measurement points significantly improves the accuracy of the RTA, $\overline{\text{RE}_{\text{ave}}}$ is 4.80%, 4.02%, and 2.81%, respectively. The 3-SOC scheme already has good accuracy. The 5-SOC scheme provides higher accuracy but also requires more data. The 4-SOC scheme strikes a balance between accuracy and demand for data.

### E. Online Heat Generation Model Based on RTA

The heat generation equation was first proposed by Mevewalla et al. [29] based on the law of conservation of energy as follows:

$$Q = \left( IV - \sum_l I_l U_{l,\text{avg}} \right) + \sum_l I_l T d \frac{U_{l,\text{avg}}}{\partial T} + M C_p \frac{dT}{dt} \tag{16}$$

where $Q$ represents the battery heat generation rate, $I$ represents the current, $V$ represents the battery terminal voltage, $I_l$ represents the partial current of electrode reaction $l$, $U_{l,\text{avg}}$ represents the theoretical open-circuit potential for reaction $l$, $T$ represents the battery temperature, $M$ represents the battery mass, and $C_p$ represents the specific heat capacity. However, owing to the complexity and the uncertainty of its complex parameters, Yang et al. [30] simplified (16) as follows:

$$Q = I\left(V - U_{\text{OCV}}\right) + IT\frac{dU_{\text{OCV}}}{dT} \tag{17}$$

where $U_{\text{OCV}}$ represents the battery open circuit voltage (OCV), and $dU_{\text{OCV}}/dT$ represents the entropy heat coefficient. In (17), the first part of the right is irreversible heat and the second is reversible heat. Moreover, (17) can be conducted to the following equation according to the Ohm's law [31]:

$$Q = I^2 R_T + IT\frac{dU_{\text{OCV}}}{dT} \tag{18}$$

where $R_T$ represents the total resistance of the battery; it is different at different SOCs and temperatures. The resistance general expression can obtain the resistance at any SOC and temperature points, and the RTA realizes self-adaptive updating

TABLE III
ERRORS AND VARIANCE OF THE 3-SOC SCHEMES

| Schemes | NCM622 | NCM111 | NCM523 | NCM811 | LFP (8 Ah) | LFP (25 Ah) | $\overline{RE_{ave}}$ | $V_{ar}$ |
|---|---|---|---|---|---|---|---|---|
| [90%, 20%, 10%] | 7.73% | 7.42% | 5.00% | 6.23% | 10.22% | 7.67% | 7.38% | 0.03% |
| [90%, 30%, 10%] | 3.43% | 6.09% | 3.34% | 5.79% | 6.83% | 8.44% | 5.65% | 0.03% |
| [90%, 40%, 10%] | 3.32% | 5.63% | 3.52% | 4.82% | 5.76% | 5.70% | 4.80% | 0.01% |
| [90%, 50%, 10%] | 3.66% | 8.41% | 3.80% | 4.88% | 4.67% | 5.08% | 5.08% | 0.02% |
| [90%, 60%, 10%] | 4.12% | 6.05% | 4.07% | 5.53% | 6.35% | 8.30% | 5.74% | 0.02% |
| [90%, 70%, 10%] | 4.06% | 7.33% | 3.55% | 5.22% | 6.82% | 5.18% | 5.36% | 0.02% |
| [90%, 80%, 10%] | 5.71% | 14.57% | 3.81% | 4.88% | 5.72% | 6.09% | 6.80% | 0.13% |

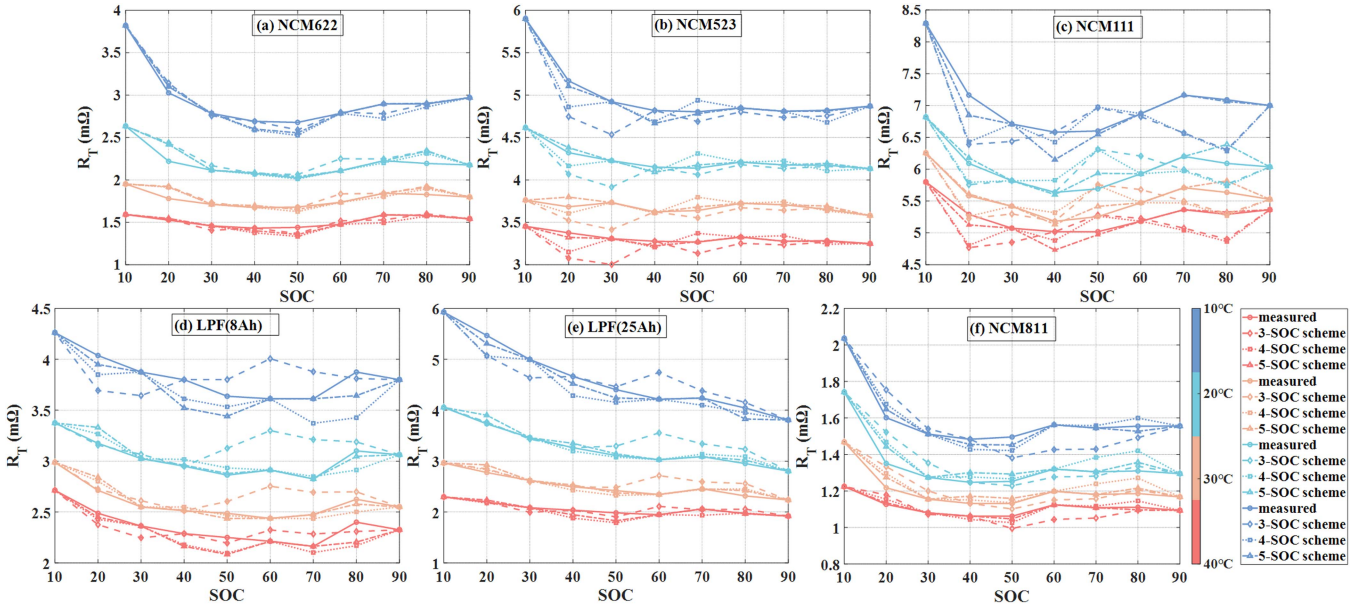


Fig. 8. Resistances value contrast with RTA values and real values. (a) NCM622. (b) NCM523. (c) NCM111. (d) LPF(8Ah). (e) LPF (25Ah). (f)NCM811.

TABLE IV
ERRORS AND VARIANCE OF THE OPTIMAL 4-SOC SCHEME AND 5-SOC SCHEME

| Battery | 4-SOC scheme [90%, 60%, 30%, 10%] | 5-SOC scheme [90%, 70, 60%, 30%, 10%] |
|---|---|---|
| NCM622 | 3.54% | 3.28% |
| NCM111 | 6.30% | 2.60% |
| NCM523 | 2.50% | 1.16% |
| NCM811 | 3.78% | 2.76% |
| LFP (8 Ah) | 4.19% | 3.74% |
| LFP (25 Ah) | 3.81% | 3.30% |
| $\overline{RE_{ave}}$ | 4.02% | 2.81% |
| $V_{ar}$ | $1.31\times10^{-4}$ | $6.83\times10^{-5}$ |

of the resistance model, which guarantees online adaptation of the heat production model.

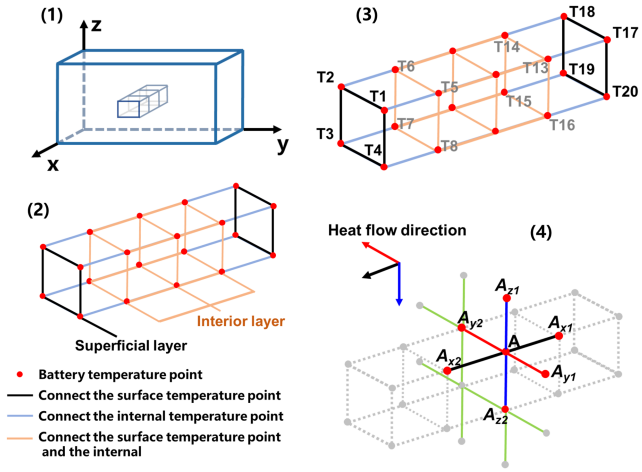


Fig. 9. Structure of the battery thermal resistance network. (1) Microstructure in the battery. (2) Superficial layer and the interior layer of the microstructure. (3) Thermal nodes of the microstructure. (4) Heat conduction of point A.

## IV. 3-D THERMAL MODEL BASED ON THERMAL RESISTANCE NETWORK

### A. 3-D Thermal Conduction Model

To construct an online application of the thermal model, a low-computation online heat conduction model is another key issue that needs to be addressed. To realize a reconstruction of the battery 3-D temperature field, the TRN is leveraged to simplify the heat conduction calculation in the battery. As shown in Fig. 9(1), the battery is cut into microstructures. One of the microstructures along the thickness direction ($x$-axis) is shown in Fig. 9(2). The microstructure includes the superficial layer and the interior layer; the red nodes represent the thermal nodes; similarly, the thermal nodes include superficial nodes [such as

T1, T2, T3, and T4 in Fig. 9(3)] and the interior nodes (such as T5, T6, T7, and T8). The heat transfer relationship between thermal nodes can be found from the labeling in Fig. 9(2), including internal heat transfer, external heat transfer, and internal to external heat transfer. It is worth noting that the external thermal node is also responsible for the heat transfer from the surface to the environment. Meanwhile, the proposed TRN structure is not immutable. For the battery with different sizes, the network may correspond to different numbers of layers and structures. In this article, the tab temperature is not taken into consideration, when a tab temperature is required, it is sufficient to classify the microstructure and set its heat production and transfer parameters.

The heat conduction in the thermal network is presented in detail utilizing point *A* in Fig. 9(4). Heat transfer in heat networks is based on the first law of thermodynamics. Therefore, the temperature-changing rate of point *A* can be constituted as

$$M_A C_p \frac{dT_A}{dt} = Q_A + (Q_{\text{exc},x1} + Q_{\text{exc},y1} + Q_{\text{exc},z1}) - (Q_{\text{exc},x2} + Q_{\text{exc},y2} + Q_{\text{exc},z2}) \tag{19}$$

where $M_A$ is the mass of zone A, $C_p$ is the specific heat capacity of the battery, $T_A$ is the average temperature of zone *A*, *t* is time, $Q_A$ is the heat generation of zone *A*, $Q_{\text{exc}}$ is the heat exchange between the adjacent regions of zone A, and the subscripts represent the adjacent regions, such as $A_{x1}, A_{x2}, A_{y1}, A_{y2}, A_{z1}$, and $A_{z2}$.

$Q_{\text{exc}}$ in (19) is the heat exchange between the adjacent regions, and it also is the heat conduction process. Thus, according to the law of thermal conduction, $Q_{\text{exc}}$ can be expressed by the temperature difference and the thermal resistance $R_t$ as

$$Q_{\text{exc}} = \frac{\Delta T}{R_t} \tag{20}$$

where $\Delta T$ is the temperature difference between zone A and the adjacent regions, and $R_t$ is the thermal resistance between zone A and the adjacent regions. Therefore, (19) can be rewritten as

$$\rho V_A C_p \frac{dT_A}{dt} = Q_A + \left(\frac{T_{Ax1} - T_A}{R_{t,\,x1}} + \frac{T_{Ay1} - T_A}{R_{t,y1}} + \frac{T_{Az1} - T_A}{R_{t,z1}}\right) - \left(\frac{T_{Ax2} - T_A}{R_{t,x2}} + \frac{T_{Ay2} - T_A}{R_{t,y2}} + \frac{T_{Az2} - T_A}{R_{t,z2}}\right) \tag{21}$$

where $\rho$ is the density of the battery, and $V_A$ is the volume. The thermal resistance $R_t$ can be calculated by the following:

$$R_t = \frac{d}{s \cdot k} \tag{22}$$

where *d* is the effective distance between the microstructure *A* and other microstructures, *s* is the surface area, and *k* is the coefficient of thermal conductivity. Due to the anisotropic nature of the battery, the *v*alues of *k* along the three axes are different. Moreover, the thermal resistance of the surface thermal nodes to the environment is expressed as

$$R_t = \frac{1}{s \cdot h} \tag{23}$$

where *h* is the heat exchange coefficient between the battery and the environment.

Substitute heat generation (18) into (21), the temperature of point *A* in the thermal conduction network can be calculated as

$$\begin{aligned} T_{A,t+1} &= T_A\left[1 - C\cdot\left(\frac{1}{R_{t,x1}} + \frac{1}{R_{t,x2}} + \frac{1}{R_{t,y1}} + \frac{1}{R_{t,y2}}\frac{1}{R_{t,z1}} + \frac{1}{R_{t,z2}}\right)\right] \\ &+ C\left[\frac{T_{Ax1,t}}{R_{t,x1}} + \frac{T_{Ax2,t}}{R_{t,x2}} + \frac{T_{Ay1,t}}{R_{t,y1}} + \frac{T_{Ay2,t}}{R_{t,y2}} + \frac{T_{Az1,t}}{R_{t,z1}} + \frac{T_{Az2,t}}{R_{t,z2}}\right] \\ &+ C\left[I^2 R_T + IT\frac{dU_{\text{OCV}}}{dT}\right] \end{aligned} \tag{24}$$

where *C* can be expressed as

$$C = \frac{\Delta t}{\rho \cdot V_A \cdot C_P}. \tag{25}$$

### B. Parameters for Thermal Model

In Section III-D, the heat generation model has two critical parameters, the resistance and the entropy heat coefficient. The resistance is updated by the RTA, and the entropy heat coefficients are acquired by experimental testing. Meanwhile, for the heat conduction model, the heat exchange coefficient determines the heat exchange between the battery and the external ambient, it is also acquired by experimental testing. These parameters are key to the accuracy of the thermal model.

The entropy heat coefficient $dU_{\text{OCV}}/dT$ is calculated by the OCV at different temperatures, and it is measured before the HPPC test. To access the entropy heat coefficient at different SOCs and temperatures, a polynomial is leveraged to fit the relationship between the entropy heat coefficient and the SOC, as shown in Fig. 10. The fitting equation is as follows:

$$\frac{dU_{\text{OCV},x}}{dT} = \sum_{i=0}^{6} c_{i,x}\,\text{SOC}^i \tag{26}$$

where *x* represents the different batteries and $c_{i,x}$ represents the coefficients of the fitting. The concrete values of $c_{i,x}$ are shown in Table V. $R^2$ of all batteries is at least 0.9605, which indicates that the fitting of the coefficients is accurate enough.

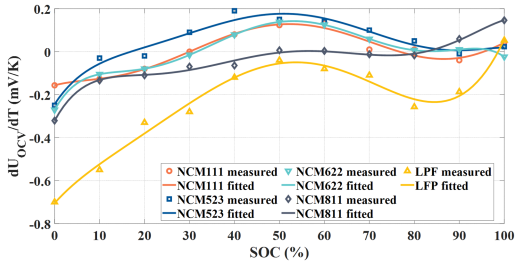


Fig. 10. Entropy heat coefficient of the battery.

TABLE V
COEFFICIENTS OF THE FITTING

| Battery | Coefficients of the fitting | $R^2$ |
|---|---|---|
| NCM111 | [-2.339×10$^{-11}$, 7.407×10$^{-9}$, -8.187×10$^{-7}$, 3.629×10$^{-5}$, - 5.470×10$^{-4}$, 0.00563, -0.157] | 0.9686 |
| NCM523 | [-3.047×10$^{-11}$, 9.895×10$^{-9}$, -1.195×10$^{-6}$, 6.674×10$^{-5}$, -0.00186, 0.0319, -0.245] | 0.9605 |
| NCM622 | [-6.835×10$^{-11}$, 2.122×10$^{-8}$, -2.459×10$^{-6}$, 1.304×10$^{-4}$, -0.00319, 0.0377, -0.271] | 1.0000 |
| NCM811 | [-4.243×10$^{-11}$, 1.377×10$^{-8}$, -1.691×10$^{-6}$, 9.826×10$^{-5}$, -0.00279, 0.0386, -0.322] | 0.9929 |
| LFP | [-1.137×10$^{-11}$, 4.7712×10$^{-9}$, -6.239×10$^{-7}$, 3.242×10$^{-5}$, -7.950×10$^{-4}$, 0.0234, -0.705] | 0.9845 |

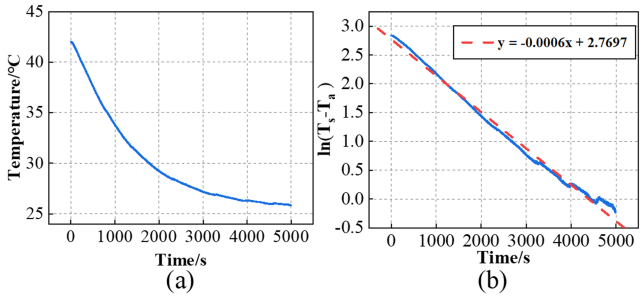


Fig. 11. Battery temperature fall for measurement of heat convection coefficient. (a) Temperature drop curve. (b) ln($T$-$T_a$) curve with time.

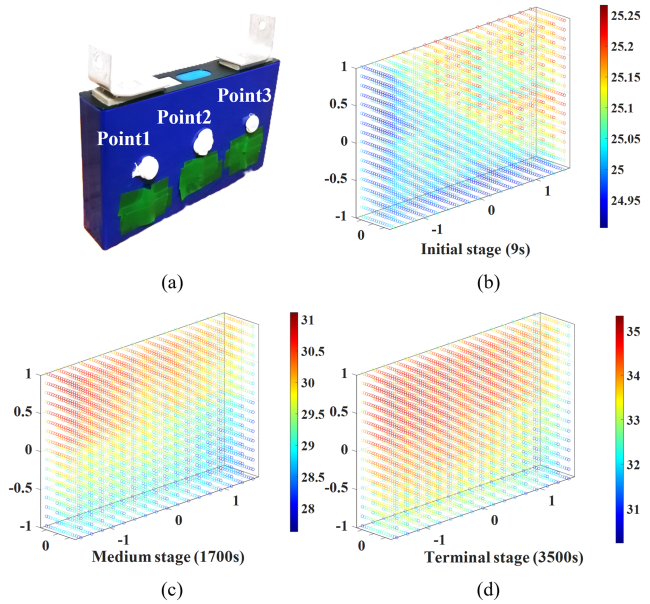


Fig. 12. Temperature field of the NCM622 at different moments. (a) Objective battery. (b) Temperature field at the initial stage. (c) Temperature field at the medium stage. (d) Temperature field at the terminal stage.

According to [32], the heat convection coefficient can be calculated from the temperature drop curve of the battery during cooling. Taking NCM811 as an example, 1 C discharge is carried out at an ambient temperature of 25 °C, and the battery is resting at the end of discharge until the temperature of the battery drops close to the temperature of the thermostat temperature. The temperature drop curve of the battery during resting is shown in Fig. 11(a). During this process, no heat is generated by the battery, the temperature can be calculated by

$$M_t C_p \frac{dT}{dt} = -h a_t (T - T_a) \tag{27}$$

where $a_t$ is the surface area of the battery, and $T_a$ is the ambient temperature. Assuming that $h$ is a constant, the following equation is obtained by converting (27):

$$\ln\ (T - T_a) = -\frac{hA}{M_t C_p} t + c \tag{28}$$

where $c$ is a constant, which is the initial value of $\ln(T - T_a)$. Equation (28) shows a linear relationship between $\ln(T - T_a)$ and time $t$. The heat convection coefficient $h$ can be calculated from the slope of the curve made by $\ln(T - T_a)$ with time $t$, as shown in Fig. 10(b), which is well linear. Therefore, the result of the calculation of $h$ for NCM811 is 16.14 W/(m$^2$·K). According to this method, the heat convection coefficients for NCM622 (51Ah), NCM111, NCM523, and LFP (25Ah) are calculated to be 19.73 W/(m$^2$·K), 10.7 W/(m$^2$·K), 15.57 W/(m$^2$·K), and 17.83 W/(m$^2$·K), respectively.

## V. APPLICATION OF ONLINE 3-D THERMAL MODEL

### A. 3-D Temperature Distribution

In Fig. 12, the 3-D temperature distribution of the NCM622 battery based on the TRN is demonstrated. Fig. 12(a) shows the objective battery, and Fig. 12(b)–(d) shows the 3-D temperature distribution of the battery at different stages. In the temperature distributions, the length, width, and height of the battery are normalized by half the height of the battery, and the center of the battery is used as the origin. The results in Fig. 12 demonstrate the ability of the TRN to reconstruct the 3-D temperature field of the battery.

Subsequently, the validation of the accuracy of temperature prediction is carried out, and the temperature collected by the thermocouple at point 2 in Fig. 12(a) is used as the measurement temperature value.

### B. Temperature Validation for Different Schemes

The basic purpose of the thermal model is to achieve accurate temperature prediction of the battery. To validate the temperature prediction precision of the proposed thermal model, the temperature of the battery is tested at 0.5 C and 1 C discharge rate and the environment temperature is set to 25 °C. The predicted temperature results are calculated by the proposed thermal model based on different resistances from three RTA schemes, including the 3-SOC scheme, the 4-SOC scheme, and the 5-SOC scheme. A computer with CPU Intel i9-13900K and RAM 64 G is employed to solve the thermal conduction network model and get the temperature distribution. All the calculation durations are no more than 0.418 s, which is significantly more efficient than the FEM. The compared results of the simulated and the predicted temperature rise are shown in Fig. 13.

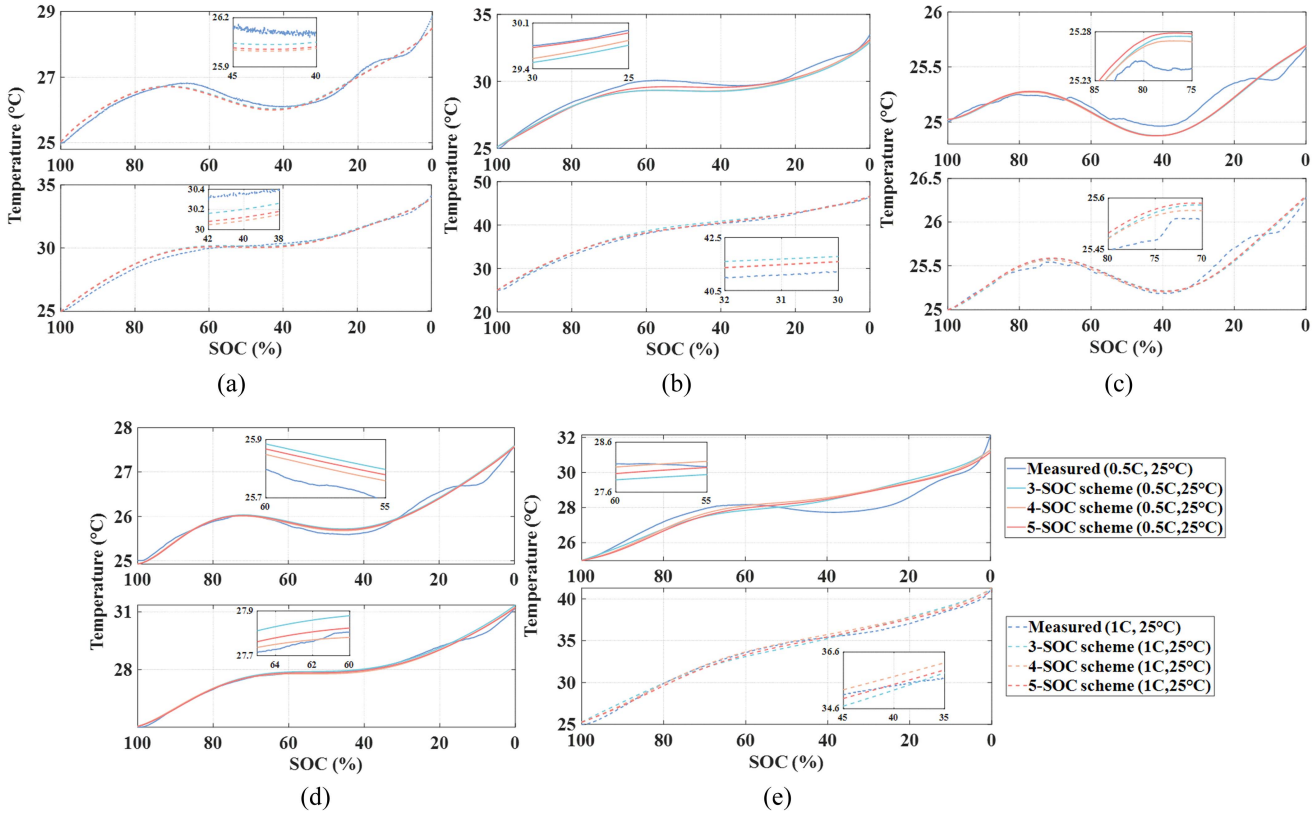


Fig. 13. Temperature prediction results of different batteries at 25 °C. (a) NCM622. (b) NCM 523. (c) NCM111. (d) LFP. (e) NCM811.

TABLE VI
MAE$_T$ OF DIFFERENT BATTERIES AT 25 °C

| Battery | MAE$_T$ at 0.5 C (°C) | | | MAE$_T$ at 1 C (°C) | | |
|---|---|---|---|---|---|---|
| | 3-SOC scheme | 4-SOC scheme | 5-SOC scheme | 3-SOC scheme | 4-SOC scheme | 5-SOC scheme |
| NCM622 | 0.0978 | 0.1097 | 0.1032 | 0.1947 | 0.1975 | 0.1835 |
| NCM523 | 0.4161 | 0.3800 | 0.2770 | 0.4601 | 0.3298 | 0.3306 |
| NCM111 | 0.0640 | 0.0641 | 0.0649 | 0.0482 | 0.0396 | 0.0476 |
| LFP | 0.0874 | 0.0747 | 0.0800 | 0.0924 | 0.0953 | 0.0713 |
| NCM811 | 0.4761 | 0.4605 | 0.4635 | 0.4379 | 0.3117 | 0.2809 |
| Mean value | 0.2283 | 0.2178 | 0.1977 | 0.2467 | 0.1948 | 0.1828 |

To assess the accuracy of the thermal model, the mean absolute error (MAE) is utilized to calculate the error between the tested value and the simulated value as

$$\mathrm{MAE}_T = \frac{1}{N}\sum_{i=1}^{N}(|T_{m,i} - T_{p,i}|) \tag{29}$$

where MAE$_T$ is the MAE between the tested temperature and the simulated temperature, $N$ is the number of the sample points, $T_{m,i}$ is the measured temperature value at the $i$th point, and $T_{p,i}$ is the predicted temperature value at the $i$th point. The statistics of MAE are presented in Table VI.

In Fig. 13, the simulated temperature rise of the five batteries at the three schemes has a similar trend to the measured value, which has a high simulation accuracy. As can be seen in Table VI, all the MAE errors of the five batteries are no more than 0.4761 °C of the NCM811. A comparison of the mean value for the different battery MAE indicates that the 5-SOC scheme has the best accuracy with the mean value of 0.1977 °C (0.5 C) and 0.1828 °C (1 C), the 4-SOC scheme is in the middle with the mean value of 0.2178 °C (0.5 C) and 0.1948 °C (1 C), and the mean value of the 3-SOC is 0.2283 °C (0.5 C) and 0.2467 °C (1 C). This is consistent with the conclusion that the 5-SOC has the best accuracy in resistance prediction. Nevertheless, for the temperature rise prediction, the 3-SOC scheme also has good accuracy with the MAE of 1.141 °C (NCM811, 0.5 C), the MAE of the 4-SOC scheme is 1.1027 °C, and the MAE of the 5-SOC scheme is 1.0498 °C. It is indicated that the proposed thermal model has a good effect on temperature rise prediction.

Comprehensively, the 4-SOC scheme demonstrates higher accuracy than the 3-SOC scheme in terms of the resistance and temperature rise evolution while requiring fewer measurement points than the 5-SOC scheme. Due to space constraints, the next temperature rise validation at 15 °C and 35 °C is commenced based on the 4-SOC scheme.

### C. Temperature Validation for Different Ambient Temperatures

The temperature rises predicted results at 15 °C and 35 °C are shown in Fig. 14, the predicted results are generally in agreement with the experimental data. Note that the battery in Fig. 14(f) is cylindrical in SOH = 85%, the battery type is NCR21700A, which is manufactured by Panasonic in Japan. Its TRN is in a cylindrical coordinate system. The maximum error is 1.515 °C of the LPF battery at the temperature of 15 °C and 1 C discharge rate, whereas its MAE is 0.3765 °C. As can be seen in Fig. 14(d), except for the end-of-discharge phase, which has a

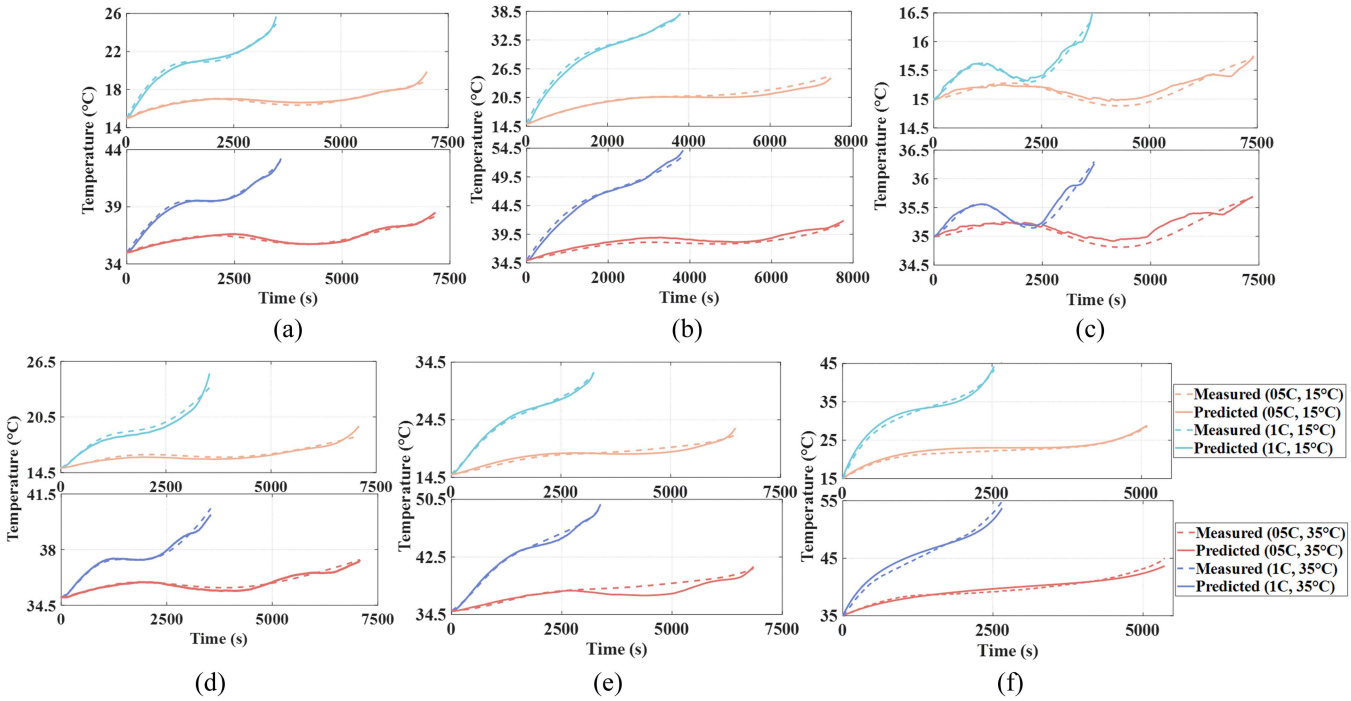


Fig. 14. Temperature prediction results of different batteries at 15 °C and 35 °C. (a) NCM622. (b) NCM 523. (c) NCM111. (d) LFP. (e) NCM811. (f) 21700 (cylindrical, SOH = 85%).

TABLE VII
MAE$_T$ OF DIFFERENT BATTERIES AT 15 °C AND 35 °C

| Battery | MAE$_T$ at 0.5 C (°C) | | MAE$_T$ at 1 C (°C) | |
|---|---|---|---|---|
| | 15°C | 35°C | 15°C | 35°C |
| NCM622 | 0.1243 | 0.0973 | 0.2209 | 0.1286 |
| NCM523 | 0.3807 | 0.4861 | 0.4658 | 0.4517 |
| NCM111 | 0.0635 | 0.0803 | 0.0407 | 0.0523 |
| LFP | 0.1829 | 0.1060 | 0.3765 | 0.1102 |
| NCM811 | 0.3930 | 0.4349 | 0.2899 | 0.2370 |
| 21700 | 0.4959 | 0.3441 | 0.7494 | 0.7362 |
| Mean value | 0.2734 | 0.2581 | 0.3572 | 0.2860 |

large error, the other parts of the prediction results are consistent with the tested temperature with a limited difference. MAE$_T$ of 0.3765 °C illustrates this point. From the statistics of MAE$_T$ in Table VII, the maximum MAE$_T$ does not exceed 0.7494 °C (21700 at 1 C, 35 °C), whereas the maximum error is not higher than 1.2105 °C, which reiterates the accuracy of the proposed thermal model. Meanwhile, the good prediction results of the temperature rise of the six cells also prove the universality of the proposed scheme.

From the perspective of all the temperature rise prediction results, the proposed RTA can be competent for the task of thermal modeling. It indicates that, with the aid of the original battery's resistance and partially available data of the target battery, achieving self-adaptive updating of thermal models is feasible.

### D. Validation of Different Methods

To validate the accuracy and computational efficiency, the proposed method is compared with the LTM and FEM thermal models under the Federal Urban Driving Schedule (FUDS) conditions, as shown in Fig. 15(a). The LTM is shown in Fig. 15(b) and the details are presented in [33]. For the FEM, the battery grid volume is 44 252, as shown in Fig. 15(b), the solver used is ANSYS Fluent 18.0 with eight cores of parallel computing. A user-defined function is implemented to dynamically transfer the unit volume heat generation rate of the battery to the solver in real time. The Gauss–Seidel iterative method is employed to solve the discretized governing equations.

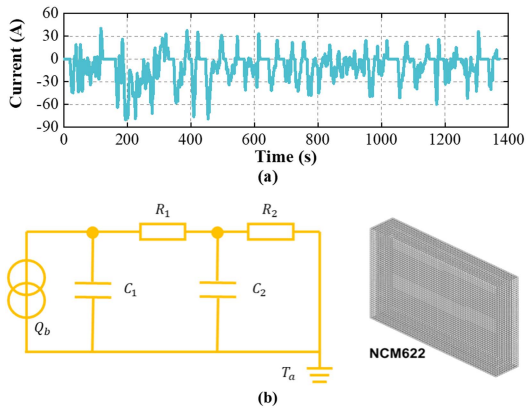


Fig. 15. Driving condition and different calculation methods for comparison among temperature solution methods. (a) FUDS condition. (b) LTM and computational grid of FEM for the NCM622.

The FUDS condition is cycled ten times, and the temperature simulation time for each method is recorded. The temperature, time, and root mean square error (RMSE) are shown in Fig. 16. Note that LTM only calculates 1-D temperatures at point 2 due

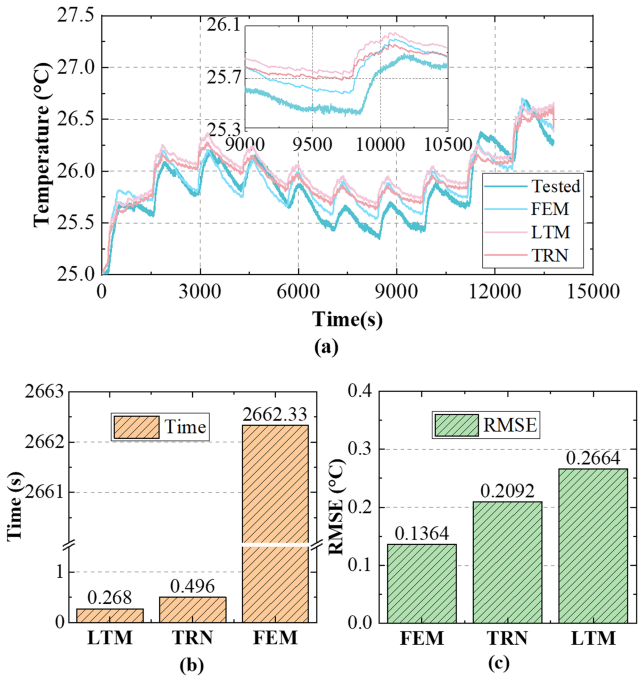


Fig. 16. Temperature, time, and RMSE of FUDS. (a) Temperature results. (b) Time of LTM, TRN and FEM. (c) RMSE of FEM, TRN and LTM.

to its simplified nature, whereas TRN and FEM calculate 3-D temperature fields.

A comparison of computation times shows that both LRM (0.268 s) and TRN (0.496 s) have faster computation speeds compared to FEM (2662.33 s). Because LTM and TRN avoid the complex partial differential operations in FEM. From the accuracy of the temperature calculations, the RMSE of the FEM, TRN, and LTM are 0.1364 °C,0.2092 °C, and 0.2664 °C. FEM is computationally intensive but has a clear accuracy advantage, whereas LTM sacrifices accuracy while reducing computational effort. TRN improves prediction accuracy while achieving 3-D temperature field monitoring in close proximity to FEM, and has the advantage of being able to be applied online. This reflects the dominance of the proposed TRN methodology.

## VI. Conclusion and Future Works

In this study, a self-adaptive 3-D online thermal model is devised. With the assistance of partial online resistance and the resistance of the original battery, the proposed RTA can achieve the resistance model self-adaptive updating for the heat generation model. Then, a TRN is established to reconstruct the 3-D temperature field. It can be solved quickly and is suitable for the online temperature rise calculation. Combining the TRN and the online updated heat generation model, a self-adaptive 3-D thermal model is proposed. Finally, the proposed method is validated on six batteries and at three temperatures. The difference between the tested resistance and the resistances conducted by the RTA is within 0.0341 mΩ. The temperature rise validation shows that the proposed 3-D thermal model can complete the calculation accurately and quickly. The computation time is no more than 0.496 s, and the maximum temperature differences have an error of no more than 1.515 °C. The results illustrate that the proposed self-adaptive 3-D online thermal model is accurate and viable.

This article focuses on a self-adaptive thermal model at the cell level. In the future, a self-adaptive thermal model for a pack is our research priority. The self-adaptive method and the TRN will be developed for battery packs and deal with the thermal model topology and heat transfer relationship of battery packs.

## References

[1] S. J. Yang, C. P. Zhang, J. C. Jiang, W. G. Zhang, L. J. Zhang, and Y. B. Wang, "Review on state-of-health of lithium-ion batteries: Characterizations, estimations and applications," *J. Cleaner Prod.*, vol. 314, Sep. 2021, Art. no. 128015.

[2] X. Sui, S. He, S. B. Vilsen, J. H. Meng, R. Teodorescu, and D. I. Stroe, "A review of non-probabilistic machine learning-based state of health estimation techniques for lithium-ion battery," *Appl. Energy*, vol. 300, Oct. 2021, Art. no. 117346.

[3] J. Shen et al., "Alternative combined co-estimation of state of charge and capacity for lithium-ion batteries in wide temperature scope," *Energy*, vol. 244, Apr. 2022, Art. no. 123236.

[4] M. K. Tran, A. DaCosta, A. Mevawalla, S. Panchal, and M. Fowler, "Comparative study of equivalent circuit models performance in four common lithium-ion batteries: LFP, NMC, LMO, NCA," *Batteries*, vol. 7, no. 3, Sep. 2021, Art. no. 51.

[5] M. S. H. Lipu et al., "A review of state of health and remaining useful life estimation methods for lithium-ion battery in electric vehicles: Challenges and recommendations," *J. Cleaner Prod.*, vol. 205, pp. 115–133, Dec. 2018.

[6] Y. S. Liu, L. C. Wang, D. Z. Li, and K. Wang, "State-of-health estimation of lithium-ion batteries based on electrochemical impedance spectroscopy: A review," *Protection Control Mod. Power Syst.*, vol. 8, no. 1, Dec. 2023, Art. no. 41.

[7] Q. Wang, B. Jiang, B. Li, and Y. Y. Yan, "A critical review of thermal management models and solutions of lithium-ion batteries for the development of pure electric vehicles," *Renewable Sustain. Energy Rev.*, vol. 64, pp. 106–128, Oct. 2016.

[8] Q. Q. Yu, Y. K. Huang, A. H. Tang, C. Wang, and W. X. Shen, "OCV-SOC-temperature relationship construction and state of charge estimation for a series-parallel lithium-ion battery pack," *IEEE Trans. Intell. Transp. Syst.*, vol. 24, no. 6, pp. 6362–6371, Jun. 2023.

[9] J. Y. Lin, X. H. Liu, S. Li, C. Zhang, and S. C. Yang, "A review on recent progress, challenges and perspective of battery thermal management system," *Int. J. Heat Mass Transf.*, vol. 167, Mar. 2021, Art. no. 120834.

[10] J. R. Chen, P. Kollmeyer, S. Panchal, Y. Masoudi, O. Gross, and A. Emadi, "Experimental results of battery power capability measurement on cells with different state of health levels," in *Proc. IEEE Transp. Electrific. Conf. Expo*, Oct. 2024, pp. 1–6.

[11] L. H. Saw et al., "Novel thermal management system using mist cooling for lithium-ion battery packs," *Appl. Energy*, vol. 223, pp. 146–158, Aug. 2018.

[12] P. Dini, A. Colicelli, and S. Saponara, "Review on modeling and SOC/SOH estimation of batteries for automotive applications," *Batteries*, vol. 10, no. 1, Jan. 2024, Art. no. 34.

[13] Y. Xie et al., "Coestimation of SOC and three-dimensional SOT for lithium-ion batteries based on distributed spatial-temporal online correction," *IEEE Trans. Ind. Electron.*, vol. 70, no. 6, pp. 5937–5948, Jun. 2023.

[14] F. Liu, D. Yu, C. Shao, X. H. Liu, and W. X. Su, "A review of multi-state joint estimation for lithium-ion battery: Research status and suggestions," *J. Energy Storage*, vol. 73, Dec. 2023, Art. no. 109071.

[15] J. Liu, S. Yadav, M. Salman, S. Chavan, and S. C. Kim, "Review of thermal coupled battery models and parameter identification for lithium-ion battery heat generation in EV battery thermal management system," *Int. J. Heat Mass Transf.*, vol. 218, Jan. 2024, Art. no. 124748.

[16] V. Mali, R. Saxena, K. Kumar, A. Kalam, and B. Tripathi, "Review on battery thermal management systems for energy-efficient electric vehicles," *Renewable Sustain. Energy Rev.*, vol. 151, Nov. 2021, Art. no. 111611.

[17] H. T. Shi et al., "A novel lumped thermal characteristic modeling strategy for the online adaptive temperature and parameter co-estimation of vehicle lithium-ion batteries," *J. Energy Storage*, vol. 50, Jun. 2022, Art. no. 104309.

[18] J. H. Li, G. X. Bai, J. Yan, and J. P. Gu, "On-line parameter identification and SOC estimation of nonlinear model of lithium-ion battery based on Wiener structure," *J. Energy Storage*, vol. 92, Jul. 2024, Art. no. 112094.
[19] S. L. Wang, C. Wang, P. Takyi-Aninakwa, S. Y. Jin, C. Fernandez, and Q. Huang, "An improved parameter identification and radial basis correction-differential support vector machine strategies for state-of-charge estimation of urban-transportation-electric-vehicle lithium-ion batteries," *J. Energy Storage*, vol. 80, Mar. 2024, Art. no. 110222.
[20] J. He, M. S. Hosen, R. Youssef, T. Kalogiannis, J. Van Mierlo, and M. Berecibar, "A lumped electro-thermal model for a battery module with a novel hybrid cooling system," *Appl. Thermal Eng.*, vol. 221, Feb. 2023, Art. no. 119874.
[21] S. Song et al., "Lifetime prediction of lithium-ion capacitors using electro-thermal-aging co-simulation platform," *J. Energy Storage*, vol. 85, Apr. 2024, Art. no. 111088.
[22] R. R. Richardson and D. A. Howey, "Sensorless battery internal temperature estimation using a Kalman filter with impedance measurement," *IEEE Trans. Sustain. Energy*, vol. 6, no. 4, pp. 1190–1199, Oct. 2015.
[23] Y. Xie, X. Wang, X. S. Hu, W. Li, Y. J. Zhang, and X. K. Lin, "An enhanced electro-thermal model for EV battery packs considering current distribution in parallel branches," *IEEE Trans. Power Electron.*, vol. 37, no. 1, pp. 1027–1043, Jan. 2022.
[24] A. H. Pordanjani et al., "Thermo-electrochemical simulation of the cooling process in a compact battery pack considering various configurations," *J. Power Sources*, vol. 553, Jan. 2023, Art. no. 232112.
[25] J. G. Zhu et al., "An improved electro-thermal battery model complemented by current dependent parameters for vehicular low temperature application," *Appl. Energy*, vol. 248, pp. 149–161, Aug. 2019.
[26] W. Choi, H. C. Shin, J. M. Kim, J. Y. Choi, and W. S. Yoon, "Modeling and applications of electrochemical impedance spectroscopy (EIS) for lithium-ion batteries," *J. Electrochem. Sci. Technol.*, vol. 11, no. 1, pp. 1–13, Feb. 2020.
[27] W. Li, Y. Xie, K. L. Liu, R. Yang, B. Chen, and Y. J. Zhang, "An enhanced thermal model with virtual resistance technique for pouch batteries at low temperature and high current rates," *IEEE J. Emerg. Sel. Topics Power Electron.*, vol. 11, no. 1, pp. 44–56, Feb. 2023.
[28] D. Pan et al., "Evaluating the accuracy of electro-thermal coupling model in lithium-ion battery via altering internal resistance acquisition methods," *J. Power Sources*, vol. 463, Jul. 2020, Art. no. 228174.
[29] A. Mevawalla, Y. Shabeer, M. K. Tran, S. Panchal, M. Fowler, and R. Fraser, "Thermal modelling utilizing multiple experimentally measurable parameters," *Batteries*, vol. 8, no. 10, Oct. 2022, Art. no. 147.
[30] R. Yang, Y. Xie, K. N. Li, Y. N. Fan, R. Sun, and Y. Liu, "An enhanced electro-thermal coupled model with lithium plating detection for lithium-ion battery at low temperatures," *IEEE Trans. Transp. Electrific.*, vol. 10, no. 1, pp. 720–734, Mar. 2024.
[31] R. Yang et al., "Comparative study on the thermal characteristics of solid-state lithium-ion batteries," *IEEE Trans. Transp. Electrific.*, vol. 10, no. 1, pp. 1541–1557, Mar. 2024.
[32] H. Ge, J. Huang, J. B. Zhang, and Z. Li, "Temperature-adaptive alternating current preheating of lithium-ion batteries with lithium deposition prevention," *J. Electrochem. Soc.*, vol. 163, no. 2, Jan. 2016, Art. no. A290.
[33] J. W. Shen, Z. Zhang, S. Q. Shen, Y. J. Zhang, Z. Chen, and Y. G. Liu, "Accurate state of temperature estimation for lithium-Ion batteries based on square root cubature Kalman filter," *Appl. Thermal Eng.*, vol. 242, Apr. 2024, Art. no. 122452.

**Yi Xie** (Member, IEEE) received the B.E. degree in power engineering from North China Electrical Power University, Beijing, China, in 2006, and the Ph.D. degree in thermal power engineering from the School of Energy and Power Engineering, Beihang University, Beijing, China, in 2012.

He is currently an Associate Professor with the College of Mechanical and Vehicle Engineering, Chongqing University, Chongqing, China. He has led and has been involved in more than 15 research projects, including the National Key R&D Program and the National Natural Science Foundation of China. He has authored or co-authored more than 30 research papers. His research interests include the thermal management of lithium-ion batteries, thermal management of electric vehicles, and intelligent air conditioning systems for vehicles.

**Wensai Ma** received the M.S. degree from the Kunming University of Science and Technology, Kunming, China, in 2023. He is currently working toward the Ph.D. degree in mechanical engineering with the College of Mechanical and Vehicle Engineering, Chongqing University.

His research interests include battery management systems and battery status estimation for electric vehicles.

**Wei Li** (Member, IEEE) received the B.E. degree in automotive engineering from Taiyuan University of Technology, Taiyuan, China, in 2016, and the Ph.D. degree in mechanical engineering with the College of Mechanical and Vehicle Engineering, Chongqing University, Chongqing, China, 2023.

He is currently a research fellow with the Department of Mechanical Engineering at the National University of Singapore. His research interests include modeling, multiple status estimation, data optimization, and advanced machine learning.

**Rui Yang** received the B.E. degree in automotive engineering from Nanjing Agricultural University, Nanjing, China, in 2019. She is currently working toward the Ph.D. degree in power engineering and engineering thermophysics with the School of Energy and Power Engineering, Chongqing University, Chongqing, China.

**Xiaoqiong Hu** received the B.E. degree in mechanical engineering from Sichuan Agricultural University, Yaan, China, in 2006.

Her current research focuses on the application of artificial intelligence algorithms in transportation and vehicles.

**Yonggang Luo** received the B.E. degree in mechanical engineering from Shandong University, Jinan, China, in 2014, and the Ph.D. degree from Purdue University, West Lafayette, IN, USA, in 2020.

He is currently the Chief Engineer with the Department of AI Application in Cockpits, Chongqing Changan Automobile, Chongqing, China. His current research focuses on the application of artificial intelligence algorithms in vehicles.

**Yangjun Zhang** received the B.E. degree in thermal engineering, and the M.S. and Ph.D. degrees in engine engineering from Beihang University, Beijing, China, in 1989, 1992, and 1995, respectively. He is currently a Professor with Tsinghua University, Beijing, China. He is also a distinguished professor of the Changjiang Scholars Program. His research interests include engine turbo systems and flow control, turbocharged internal combustion (IC) engines, turbo compound fuel cell engines, and turboelectric propulsion power systems for automotive and aeronautical applications.

Prof. Zhang is one of the Editors-in-Chief of the *International Journal of Fluid Machinery and Systems*.